

Application of modeling techniques for ultrasonic austenitic weld inspection

K.J. Langenberg^{a,*}, R. Hannemann^a, T. Kaczorowski^a, R. Marklein^a, B. Koehler^b, C. Schurig^b, F. Walte^b

^aDepartment of Electrical Engineering, University of Kassel, D-34109 Kassel, Germany

^bFraunhofer Institute for Nondestructive Testing, EADQ and IZFP, Dresden and Saarbrücken, Germany

Abstract

After a brief discussion of the fundamental equations of elastic wave propagation in anisotropic (transversely isotropic) materials and their basic solutions in terms of plane waves and Green functions, we point out and demonstrate the usefulness of Huygens' principle in conjunction with the results obtained by the numerical Elastodynamic Finite Integration Technique (EFIT)-code for an intuitive physical understanding of ultrasound propagation in austenitic steel. EFIT is briefly explained and then validated against a weld transmission experiment; applications to pulse echo simulations for various canonical and real-life geometries and structures with and without backwall entering notches are to follow. Further, we have been able to confirm the existence of the second qSV-wave, as predicted by plane wave theory, through EFIT-modeling as well as experiments. © 2000 Elsevier Science Ltd. All rights reserved.

Keywords: Elastodynamic Finite Integration Technique; Ultrasonic nondestructive evaluation; Anisotropic welds; Huygens' principle in anisotropic media

1. As an introduction: the mathematical setting

1.1. Governing equations, plane waves, Green's functions, Huygens' principle

1.1.1. Governing equations

Ultrasonic inspection of solids as a particular method of NDE (Nondestructive Evaluation) relies on elastic waves in $\mathbf{R}t$ -space: \mathbf{R} is the vector of position and t is time. For modeling purposes, the underlying governing equations have to be solved. In our case of linear elastodynamics these are the equation of motion and the deformation rate equation [1–5]:

$$\frac{\partial}{\partial t} \mathbf{j}(\mathbf{R}, t) = \nabla \cdot \underline{\underline{\mathbf{T}}}(\mathbf{R}, t) + \underline{\underline{\mathbf{f}}}(\mathbf{R}, t), \quad (1)$$

$$\frac{\partial}{\partial t} \underline{\underline{\mathbf{S}}}(\mathbf{R}, t) = \frac{1}{2} \{ \nabla \underline{\underline{\mathbf{v}}}(\mathbf{R}, t) + [\nabla \underline{\underline{\mathbf{v}}}(\mathbf{R}, t)]^{21} \} + \underline{\underline{\mathbf{h}}}(\mathbf{R}, t), \quad (2)$$

where the elastic wavefield is characterized by the momentum density $\mathbf{j}(\mathbf{R}, t)$, the second rank stress tensor $\underline{\underline{\mathbf{T}}}(\mathbf{R}, t)$, the second rank strain tensor $\underline{\underline{\mathbf{S}}}(\mathbf{R}, t)$, and the particle velocity $\underline{\underline{\mathbf{v}}}(\mathbf{R}, t)$; the upper indicial notation indicates the transpose of a dyadic, and ∇ is the del-operator: it stands for the divergence when applied by a dot-product, it stands for the

curl when applied by a cross-product, and it stands for the gradient (dyadic) when applied without dot or cross, i.e. as a dyadic product. The quantities $\underline{\underline{\mathbf{f}}}(\mathbf{R}, t)$, $\underline{\underline{\mathbf{h}}}(\mathbf{R}, t)$ —the volume force density and the injected deformation rate—account for external (given, prescribed) sources, i.e. transducers.

On a boundary S between two homogeneous materials (1) and (2) with different elastic properties, the governing equations reduce to boundary conditions for $\mathbf{R} \in S$:

$$\mathbf{n} \cdot [\underline{\underline{\mathbf{T}}}^{(2)}(\mathbf{R}, t) - \underline{\underline{\mathbf{T}}}^{(1)}(\mathbf{R}, t)] = -\underline{\underline{\mathbf{t}}}(\mathbf{R}, t), \quad (3)$$

$$\begin{aligned} \frac{1}{2} [\underline{\underline{\mathbf{nv}}}^{(2)}(\mathbf{R}, t) + \underline{\underline{\mathbf{v}}}^{(2)}(\mathbf{R}, t)\mathbf{n} - \underline{\underline{\mathbf{nv}}}^{(1)}(\mathbf{R}, t) - \underline{\underline{\mathbf{v}}}^{(1)}(\mathbf{R}, t)\mathbf{n}] \\ = -\underline{\underline{\mathbf{g}}}(\mathbf{R}, t), \end{aligned} \quad (4)$$

where $\underline{\underline{\mathbf{t}}}$ and $\underline{\underline{\mathbf{g}}}$ are given surface densities of force and injected deformation rate, respectively; \mathbf{n} is the normal unit-vector on S pointing from material (1) into material (2). If material (1) supports no elastic wave field, we have instead of Eqs. (3) and (4)—the index (2) becomes superfluous

$$\mathbf{n} \cdot \underline{\underline{\mathbf{T}}}(\mathbf{R}, t) = -\underline{\underline{\mathbf{t}}}(\mathbf{R}, t), \quad \mathbf{R} \in S, \quad (5)$$

$$\frac{1}{2} [\underline{\underline{\mathbf{nv}}}(\mathbf{R}, t) + \underline{\underline{\mathbf{v}}}(\mathbf{R}, t)\mathbf{n}] = -\underline{\underline{\mathbf{g}}}(\mathbf{R}, t), \quad \mathbf{R} \in S. \quad (6)$$

The case of material (1) being vacuum is particularly important in NDE, it yields the stress-free boundary

* Corresponding author.

E-mail address: langenberg@tet.e-technik.uni-kassel.de (K.J. Langenberg).

conditions

$$\underline{\mathbf{n}} \cdot \underline{\mathbf{T}}(\underline{\mathbf{R}}, t) = \underline{0}, \quad \underline{\mathbf{R}} \in S, \quad (7)$$

$$\frac{1}{2} [\underline{\mathbf{n}} \underline{\mathbf{v}}(\underline{\mathbf{R}}, t) + \underline{\mathbf{v}}(\underline{\mathbf{R}}, t) \underline{\mathbf{n}}] = -\underline{\mathbf{g}}(\underline{\mathbf{R}}, t), \quad \underline{\mathbf{R}} \in S. \quad (8)$$

Here, $\underline{\mathbf{g}}(\underline{\mathbf{R}}, t)$ in Eq. (8) can no longer be *prescribed* arbitrarily, it has to be *determined* enforcing the boundary condition (7) for a particular solution of the governing equations; then $\underline{\mathbf{g}}(\underline{\mathbf{R}}, t)$ turns out to be an equivalent, field-dependent source of the secondary field because of the scattering or diffraction of the incident field by the surface S .

Considered as such, Eqs. (1) and (2) are still useless, because each equation contains different physical fields: constitutive equations are required! We apply

$$\underline{\mathbf{j}}(\underline{\mathbf{R}}, t) = \rho(\underline{\mathbf{R}}) \underline{\mathbf{v}}(\underline{\mathbf{R}}, t) \quad (9)$$

together with Hooke's law of linear elastodynamics

$$\underline{\underline{\mathbf{S}}}(\underline{\mathbf{R}}, t) = \underline{\underline{\mathbf{s}}}(\underline{\mathbf{R}}) : \underline{\underline{\mathbf{T}}}(\underline{\mathbf{R}}, t) \quad (10)$$

introducing the mass density $\rho(\underline{\mathbf{R}})$ and $\underline{\underline{\mathbf{s}}}(\underline{\mathbf{R}})$, the compliance tensor of rank four. By symmetry of $\underline{\underline{\mathbf{S}}}$ and $\underline{\underline{\mathbf{T}}}$, as well as recognizing the elastodynamic Poynting-theorem for the Poynting-vector

$$\underline{\underline{\mathbf{S}}}(\underline{\mathbf{R}}, t) = -\underline{\mathbf{v}}(\underline{\mathbf{R}}, t) \cdot \underline{\underline{\mathbf{T}}}(\underline{\mathbf{R}}, t), \quad (11)$$

the 81 components of $\underline{\underline{\mathbf{s}}}(\underline{\mathbf{R}})$ reduce to only 21 independent ones. The particular constitutive equations refer to linear, anisotropic, inhomogeneous, time-invariant, locally and instantaneously reacting materials, i.e. dissipation and, therefore, frequency dependence is not included.

Inverting Hooke's law defining the stiffness tensor $\underline{\underline{\mathbf{c}}}(\underline{\mathbf{R}})$ through

$$\underline{\underline{\mathbf{T}}}(\underline{\mathbf{R}}, t) = \underline{\underline{\mathbf{c}}}(\underline{\mathbf{R}}) : \underline{\underline{\mathbf{S}}}(\underline{\mathbf{R}}, t) \quad (12)$$

we obtain a single partial differential equation for $\underline{\mathbf{v}}(\underline{\mathbf{R}}, t)$:

$$\begin{aligned} \underline{\underline{\mathbf{c}}}(\underline{\mathbf{R}}) : \nabla \underline{\mathbf{v}}(\underline{\mathbf{R}}, t) - \rho(\underline{\mathbf{R}}) \frac{\partial^2}{\partial t^2} \underline{\mathbf{v}}(\underline{\mathbf{R}}, t) \\ = -\frac{\partial}{\partial t} \underline{\mathbf{f}}(\underline{\mathbf{R}}, t) - \nabla \cdot \underline{\underline{\mathbf{c}}}(\underline{\mathbf{R}}) : \underline{\underline{\mathbf{h}}}(\underline{\mathbf{R}}, t). \end{aligned} \quad (13)$$

Three solution categories for this equation can be defined:

- solutions of the homogeneous equation;
- solutions of the inhomogeneous equation for given sources in "free space": this is the transducer problem in an elastic material of infinite extent;
- solutions of the inhomogeneous equation in the presence of boundaries and scatterers: this is—in our case—the weld modeling problem.

1.1.2. Plane waves

Solutions of the *homogeneous* Eq. (13) are of particular interest for *homogeneous* materials (of infinite extent); they

(may) define plane waves as the fundamental building block for ultrasonic experiment interpretation.

Introducing a Fourier transform with regard to t —circular frequency ω is the conjugate variable, and j the imaginary unit—according to

$$\underline{\mathbf{v}}(\underline{\mathbf{R}}, \omega) = \int_{-\infty}^{\infty} \underline{\mathbf{v}}(\underline{\mathbf{R}}, t) e^{j\omega t} dt \quad (14)$$

as well as a three-dimensional (3D) Fourier transform with regard to the three components of $\underline{\mathbf{R}}$ in a cartesian coordinate system x, y, z according to

$$\underline{\mathbf{v}}(\underline{\mathbf{K}}, \omega) = \int_{-\infty}^{\infty} \int_{-\infty}^{\infty} \int_{-\infty}^{\infty} \underline{\mathbf{v}}(\underline{\mathbf{R}}, \omega) e^{-j\underline{\mathbf{K}} \cdot \underline{\mathbf{R}}} d^3 \underline{\mathbf{R}} \quad (15)$$

yields

$$(\underline{\underline{\mathbf{c}}} : \underline{\underline{\mathbf{c}}} : \underline{\underline{\mathbf{K}}}) \cdot \underline{\mathbf{v}}(\underline{\mathbf{K}}, \omega) = \rho \omega^2 \underline{\mathbf{v}}(\underline{\mathbf{K}}, \omega) \quad (16)$$

instead of Eq. (13). The Fourier vector $\underline{\mathbf{K}}$ has cartesian components K_x, K_y, K_z . Eq. (16) defines an eigenvalue problem for the eigenvalues $\omega(\underline{\mathbf{K}})$ and the corresponding eigenvectors $\underline{\mathbf{v}}(\underline{\mathbf{K}}, \omega)$. Two special cases are really important: the isotropic material for the sake of simplicity, and the transversely isotropic material as our model for anisotropic welds. In the first case we have

$$\underline{\underline{\mathbf{c}}} = \lambda \underline{\underline{\mathbf{I}}} + \mu (\underline{\underline{\mathbf{I}}}^{1342} + \underline{\underline{\mathbf{I}}}^{1324}) \quad (17)$$

with Lamé's constants λ and μ — $\underline{\underline{\mathbf{I}}}$ is the dyadic idemfactor, $\underline{\underline{\mathbf{I}}}$ its dyadic product with itself, and the upper indicial notation indicates transposition of the elements of $\underline{\underline{\mathbf{I}}}$. Solving the eigenvalue problem (16) for (17) we obtain the single eigenvalue

$$\omega(\underline{\mathbf{K}}) = \sqrt{\frac{\lambda + 2\mu}{\rho}} \underline{\mathbf{K}} \cdot \underline{\mathbf{K}} = K c_p, \quad (18)$$

which restricts—for a given circular frequency ω —the magnitude K of the Fourier vector to the wavenumber $k_p = K = \omega/c_p$ of pressure (primary) waves with the phase velocity c_p , and a double eigenvalues

$$\omega(\underline{\mathbf{K}}) = \sqrt{\frac{\mu}{\rho}} \underline{\mathbf{K}} \cdot \underline{\mathbf{K}} = K c_s \quad (19)$$

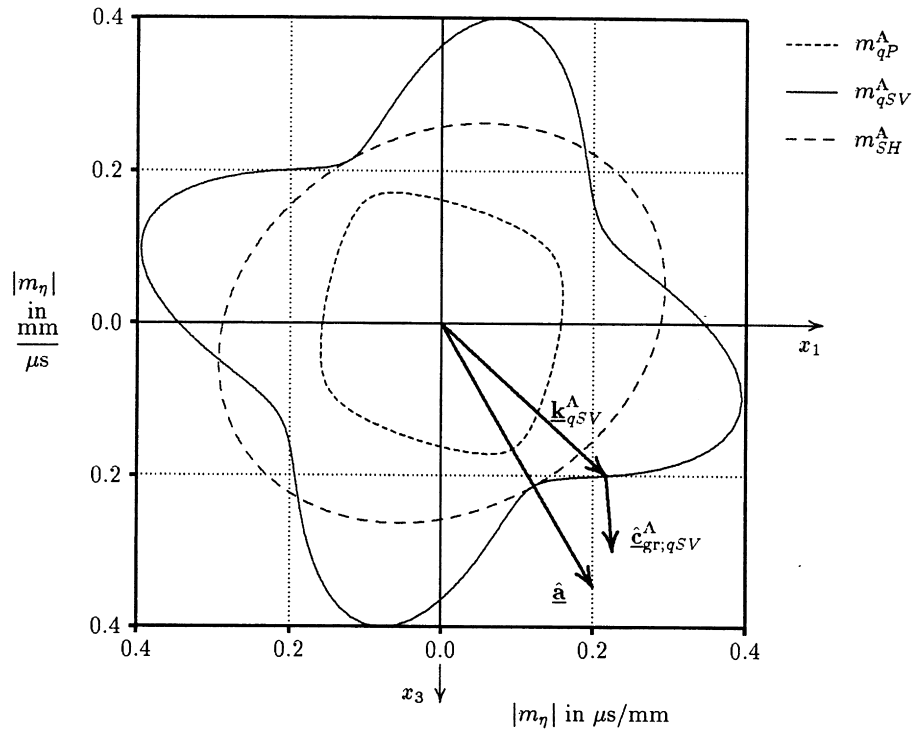
with the wavenumber $k_s = K = \omega/c_s$ and the phase velocity c_s of shear (secondary) waves. For the eigenvectors it turns out, that pressure wave Fourier spectra are longitudinally polarized, i.e. a single plane wave component $\underline{\mathbf{v}}_0(\underline{\mathbf{K}}, \omega)$ out of the Fourier spectrum of $\underline{\mathbf{v}}(\underline{\mathbf{K}}, \omega)$ with unit-propagation vector $\underline{\hat{\mathbf{K}}}$ according to

$$\underline{\mathbf{v}}(\underline{\mathbf{R}}, \omega) = \underline{\mathbf{v}}_0(\underline{\hat{\mathbf{K}}}, \omega) e^{j k_p \underline{\hat{\mathbf{K}}} \cdot \underline{\mathbf{R}}} \quad (20)$$

must satisfy $\underline{\mathbf{v}}_0(\underline{\hat{\mathbf{K}}}, \omega) \times \underline{\hat{\mathbf{K}}} = \underline{0}$. On the other hand, shear wave Fourier spectra are transversely polarized, i.e. for

$$\underline{\mathbf{v}}(\underline{\mathbf{R}}, \omega) = \underline{\mathbf{v}}_0(\underline{\hat{\mathbf{K}}}, \omega) e^{j k_s \underline{\hat{\mathbf{K}}} \cdot \underline{\mathbf{R}}} \quad (21)$$

we have $\underline{\mathbf{v}}_0(\underline{\hat{\mathbf{K}}}, \omega) \cdot \underline{\hat{\mathbf{K}}} = 0$. As the corresponding eigenvalue

Fig. 1. Slowness diagrams $m_{qP,qSV,qSH}^A$ for austenitic steel.

appears twice, we can choose two arbitrary orthogonal transverse shear wave polarizations (usually denoted by SH—shear horizontal with $\mathbf{n} \cdot \mathbf{v}_0 = 0$ —and SV—shear vertical with $\mathbf{n} \times \mathbf{k} \cdot \mathbf{v}_0 = 0$ —which refers to an appropriately chosen reference plane with unit-normal \mathbf{n} , for instance the plane surface of a specimen or part).

The transversely isotropic material is defined as a special anisotropic material with a preference direction given by the unit-vector $\hat{\mathbf{a}}$; in the plane orthogonal to $\hat{\mathbf{a}}$ the material is assumed to be isotropic. Austenitic steel welds are very often characterized by a crystal structure, which allows for this model, and we will demonstrate that in this paper. The stiffness tensor of such a material is given by

$$\begin{aligned} \underline{\underline{\mathbf{c}}} = & \lambda_{\perp} \underline{\underline{\mathbf{I}}} + \mu_{\perp} [\underline{\underline{\mathbf{I}}} \underline{\underline{\mathbf{I}}}^{1324} + \underline{\underline{\mathbf{I}}} \underline{\underline{\mathbf{I}}}^{1342}] + [\lambda_{\perp} + 2\mu_{\perp} + \lambda_{\parallel} + 2\mu_{\parallel} \\ & - 2(\nu + 2\mu_{\parallel}) \hat{\mathbf{a}} \hat{\mathbf{a}} \hat{\mathbf{a}} \hat{\mathbf{a}} + (\nu - \lambda_{\perp})(\hat{\mathbf{a}} \hat{\mathbf{a}} + \hat{\mathbf{a}} \hat{\mathbf{a}} \hat{\mathbf{I}}) \\ & + (\mu_{\parallel} - \mu_{\perp})(\hat{\mathbf{a}} \hat{\mathbf{a}} \hat{\mathbf{I}}^{1342} + \hat{\mathbf{a}} \hat{\mathbf{a}} \hat{\mathbf{I}}^{1324} + \hat{\mathbf{a}} \hat{\mathbf{a}} \hat{\mathbf{I}}^{1342} + \hat{\mathbf{a}} \hat{\mathbf{a}} \hat{\mathbf{I}}^{1324}) \end{aligned} \quad (22)$$

thus defining five independent “Lamé-constants” [4,6]. Again, inserting Eq. (22) into Eq. (16) results in three real eigenvalues defining wavenumbers $k_{qP}(\hat{\mathbf{k}}, \hat{\mathbf{a}})$, $k_{qS1}(\hat{\mathbf{k}}, \hat{\mathbf{a}})$, $k_{qS2}(\hat{\mathbf{k}}, \hat{\mathbf{a}})$ for plane waves with (phase) propagation direction $\hat{\mathbf{k}}$. All wavenumbers are related to their respective phase velocities $c_{qP}(\hat{\mathbf{k}}, \hat{\mathbf{a}})$, $c_{qS1}(\hat{\mathbf{k}}, \hat{\mathbf{a}})$, $c_{qS2}(\hat{\mathbf{k}}, \hat{\mathbf{a}})$ through $k_{qP,qS1,qS2} = \omega/c_{qP,qS1,qS2}$, they are proportional to the slownesses $m_{\eta} = c_{\eta}^{-1}$ with $\eta = qP, qS1, qS2$. Three real eigenvalues yield three real-valued orthogonal eigenvectors accounting for the polarization of plane waves in transversely isotropic

media; none of these polarizations is, in general, either parallel or orthogonal to $\hat{\mathbf{k}}$. In the case of only weak anisotropy of the material, we observe that qP refers to a nearly longitudinally polarized pressure wave, and qS1/qS2 refer to two orthogonal transversely polarized shear waves. If, in addition, $\hat{\mathbf{a}}$ lies in the plane spanned by $\hat{\mathbf{k}}$ and the reference plane normal \mathbf{n} , i.e. in the “plane of incidence”, that is to say, if $\mathbf{n} \cdot \hat{\mathbf{a}} \times \hat{\mathbf{k}} = 0$, we can identify qS1 with SH ($\mathbf{v}_0 \cdot \mathbf{n} = 0$) and, at least approximately, qS2 with qSV ($\mathbf{v}_0 \cdot \mathbf{n} \times \hat{\mathbf{k}} = 0$).

The most important observation, yet, is the dependence of the wavenumbers and phase velocities on the direction $\hat{\mathbf{k}}$ of phase propagation. Therefore, for the three wave modes qP, qS1, qS2 we obtain for $\hat{\mathbf{a}} = \cos 60^\circ \mathbf{e}_1 + \sin 60^\circ \mathbf{e}_3$ the slowness diagrams of Fig. 1 (we have $\mathbf{n} \cdot \hat{\mathbf{a}} \times \hat{\mathbf{k}} = 0$) in the $\hat{\mathbf{a}}\mathbf{n}\hat{\mathbf{k}}$ -plane with x_1, x_3 -coordinates, hence, qS1 = SH, qS2 = qSV; we have chosen a mass density at rest of $\rho^A = 7800 \text{ kg/m}^3$ and elastic constants given in form of the stiffness matrix for $\hat{\mathbf{a}} = \mathbf{e}_1$

$$[\mathbf{c}]^A(\hat{\mathbf{a}} = \mathbf{e}_1)$$

$$= \begin{bmatrix} 216.0 & 145.0 & 145.0 & 0.0 & 0.0 & 0.0 \\ & 262.75 & 98.25 & 0.0 & 0.0 & 0.0 \\ & & 262.75 & 0.0 & 0.0 & 0.0 \\ & & & 82.25 & 0.0 & 0.0 \\ & \text{sym} & & & 129.0 & 0.0 \\ & & & & & 129.0 \end{bmatrix} \text{ GPa}$$

referring to a special austenitic steel A.

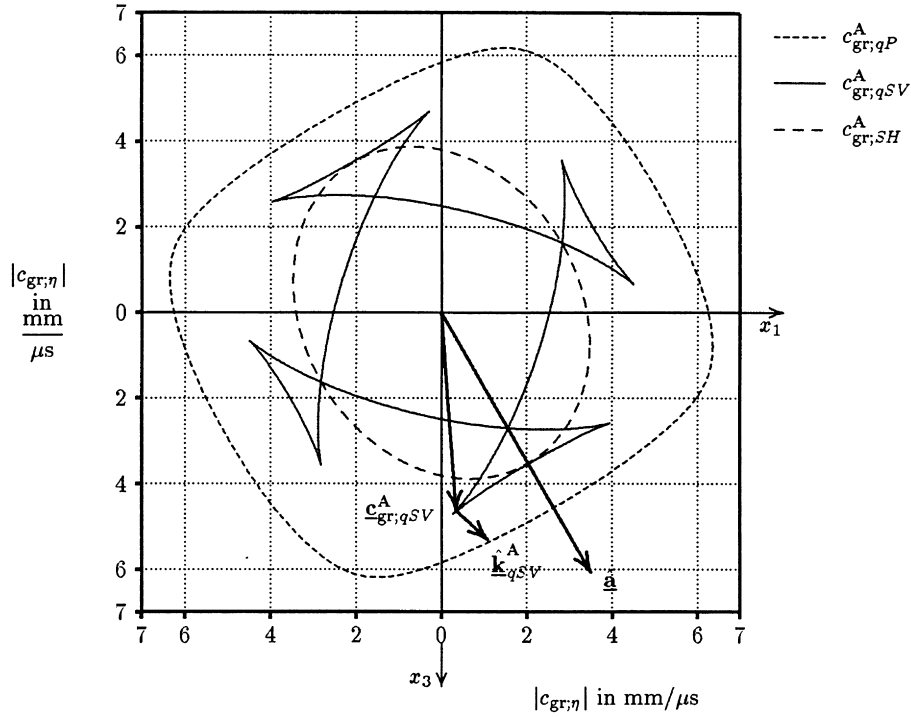


Fig. 2. Group velocity diagrams $c_{gr;qP,qSV,qSH}^A$ for austenitic steel.

Interesting enough, the group velocities $\underline{c}_{gr;qP,qS1,qS2}(\underline{\hat{k}}, \underline{\hat{a}})$ as defined by the velocity of Poynting-vector propagation not only depend upon $\underline{\hat{k}}$ as well, they are, in particular, not equal to the phase velocities, neither regarding their magnitude nor their direction, i.e. $\underline{c}_{gr;qP,qS1,qS2} \neq c_{qP,qS1,qS2} \underline{\hat{k}}$ (for instance: [6–9]). Fig. 2 shows the respective group velocity diagrams (magnitudes) complementing Fig. 1. In Fig. 1 we have also indicated the fact, that for a given phase vector, say $\underline{\hat{k}}_{pSV}$, the unit-vector of the group velocity $\underline{\hat{c}}_{gr;qSV}$ is orthogonal to the corresponding slowness diagram, and vice versa in Fig. 2: This illustrates the different directions of phase and energy propagation. But: For the *plane* wave, this different direction is not “visible”, the energy simply “slides” along the wavefront of infinite extent. Therefore, interpreting the consequences of phase and group velocity distinction for NDE transducer and scattered fields is *the* key to perform and understand ultrasonic austenitic weld modeling.

1.1.3. Green's functions, incident fields

The simplest source one can consider in a homogeneous elastic solid of infinite extent is a dyadic point source $\delta(\underline{\mathbf{R}} - \underline{\mathbf{R}}') \underline{\mathbf{I}}$ at the source point $\underline{\mathbf{R}}'$, $\delta(\underline{\mathbf{R}} - \underline{\mathbf{R}}')$ denoting the 3D delta-distribution. In the frequency domain, the resulting “wavefield” is then given by the dyadic Green function $\underline{\underline{\mathbf{G}}}(\underline{\mathbf{R}} - \underline{\mathbf{R}}', \omega)$ satisfying the accordingly inhomogeneous Fourier-transformed Eq. (13):

$$\nabla \cdot \underline{\underline{\mathbf{c}}} : \nabla \underline{\underline{\mathbf{G}}}(\underline{\mathbf{R}} - \underline{\mathbf{R}}', \omega) + \rho \omega^2 \underline{\underline{\mathbf{G}}}(\underline{\mathbf{R}} - \underline{\mathbf{R}}', \omega) = -\delta(\underline{\mathbf{R}} - \underline{\mathbf{R}}') \underline{\mathbf{I}}. \quad (23)$$

The essence of Green functions (dyadics) is, that the solution of Eq. (13) for the arbitrary volume source densities residing in the volume V_Q is just the super position of “dyadic point-source wavefields” represented by $\underline{\underline{\mathbf{G}}}(\underline{\mathbf{R}} - \underline{\mathbf{R}}', \omega)$:

$$\underline{\mathbf{v}}_i(\underline{\mathbf{R}}, \omega) = \iiint_{V_Q} [-j\omega \underline{\mathbf{f}}(\underline{\mathbf{R}}', \omega) + \nabla' \cdot \underline{\underline{\mathbf{c}}} : \underline{\underline{\mathbf{h}}}(\underline{\mathbf{R}}', \omega)] \cdot \underline{\underline{\mathbf{G}}}(\underline{\mathbf{R}} - \underline{\mathbf{R}}', \omega) d^3 \underline{\mathbf{R}}'. \quad (24)$$

We have added an index for “incident”, because Eq. (24) is an appropriate model for *incident* transducer fields, the sources $\underline{\mathbf{f}}$ and $\underline{\mathbf{h}}$ being supposed to be given: It is obvious, that this is a “Point Source Synthesis Model” for the most general case of an arbitrary anisotropic, yet homogeneous, material (of infinite extent).

For arbitrary anisotropy, the explicit solution of Eq. (23) is not known, but for the *isotropic* solid— $\underline{\underline{\mathbf{c}}}$ given by Eq. (17)—the solution is readily at hand in terms of the scalar Green functions $G_{P,S}(\underline{\mathbf{R}} - \underline{\mathbf{R}}', \omega)$ [1–3]:

$$\underline{\underline{\mathbf{G}}}(\underline{\mathbf{R}} - \underline{\mathbf{R}}', \omega) = -\frac{1}{\rho \omega^2} \nabla \nabla G_P(\underline{\mathbf{R}} - \underline{\mathbf{R}}', \omega) + \frac{1}{\rho \omega^2} (k_S^2 \underline{\underline{\mathbf{I}}} + \nabla \nabla) G_S(\underline{\mathbf{R}} - \underline{\mathbf{R}}', \omega), \quad (25)$$

where

$$G_{P,S}(\underline{\mathbf{R}} - \underline{\mathbf{R}}', \omega) = \frac{e^{jk_{P,S}|\underline{\mathbf{R}} - \underline{\mathbf{R}}'|}}{4\pi|\underline{\mathbf{R}} - \underline{\mathbf{R}}'|}. \quad (26)$$

Therefore, in this case, it is easy to visualize the “elementary elastic wavelets” (in Huygens’ terminology) for a given point source, say $\underline{\mathbf{f}}(\underline{\mathbf{R}}, \omega) = F(\omega)\delta(\underline{\mathbf{R}})\underline{\hat{\mathbf{f}}}$ and $\underline{\mathbf{h}}(\underline{\mathbf{R}}, \omega)$ being zero; $F(\omega)$ as the Fourier transform of $f(t)$ is the source spectrum and $\underline{\hat{\mathbf{f}}}$ its (unit-vector) direction.

From Eq. (25) we obtain the convolution integral

$$\underline{\mathbf{v}}_i(\underline{\mathbf{R}}, t) = \int_{-\infty}^{\infty} \frac{df(\tau)}{d\tau} \underline{\hat{\mathbf{f}}} \cdot \underline{\mathbf{G}}(\underline{\mathbf{R}}, t - \tau) d\tau, \quad (27)$$

and obviously, $\underline{\mathbf{v}}_i(\underline{\mathbf{R}}, t)$ exhibits spherical pressure and shear wavefronts with directional dependent amplitudes whose time structure, at least in the far-field, is determined by $df(t)/dt$.

Through partial integration, the $(\nabla' \cdot)$ -derivative on $\underline{\mathbf{c}} : \underline{\underline{\mathbf{h}}}(\underline{\mathbf{R}}', \omega)$ in Eq. (25) can be shifted to $\underline{\mathbf{G}}$ yielding

$$\underline{\mathbf{v}}_i(\underline{\mathbf{R}}, \omega) = \int \int \int_{V_Q} [-j\omega \underline{\mathbf{f}}(\underline{\mathbf{R}}', \omega) \cdot \underline{\mathbf{G}}(\underline{\mathbf{R}} - \underline{\mathbf{R}}', \omega) - \underline{\underline{\mathbf{h}}}(\underline{\mathbf{R}}', \omega) : \underline{\underline{\Sigma}}'(\underline{\mathbf{R}} - \underline{\mathbf{R}}', \omega)] d^3 \underline{\mathbf{R}}', \quad (28)$$

with the third rank Green tensor $\underline{\underline{\Sigma}}'$ given by

$$\underline{\underline{\Sigma}}'(\underline{\mathbf{R}} - \underline{\mathbf{R}}', \omega) = \underline{\mathbf{c}} : \nabla' \underline{\mathbf{G}}(\underline{\mathbf{R}} - \underline{\mathbf{R}}', \omega). \quad (29)$$

Eq. (29) is the starting point to argue for a Point Source Synthesis Model of *scattered* fields in terms of Huygens’ principle.

1.1.4. Huygens’ principle

Consider a scatterer—a “defect”—with surface S_c and outward normal $\underline{\mathbf{n}}_c$. We “derive” Huygens’ principle for elastic waves by intuition: First, we reduce the volume source densities $\underline{\mathbf{f}}$ and $\underline{\mathbf{h}}$ in Eq. (28) to surface source densities $\underline{\mathbf{t}}$ and $\underline{\mathbf{g}}$ located on S_c , and, second, we relate *those* to surface *fields* according to

$$\underline{\mathbf{t}}(\underline{\mathbf{R}}, \omega) = -\underline{\mathbf{n}}_c \cdot \underline{\underline{\mathbf{T}}}(\underline{\mathbf{R}}, \omega), \quad \underline{\mathbf{R}} \in S_c, \quad (30)$$

$$\underline{\mathbf{g}}(\underline{\mathbf{R}}, \omega) = -\frac{1}{2} [\underline{\mathbf{n}}_c \underline{\mathbf{v}}(\underline{\mathbf{R}}, \omega) + \underline{\mathbf{v}}(\underline{\mathbf{R}}, \omega) \underline{\mathbf{n}}_c], \quad \underline{\mathbf{R}} \in S_c, \quad (31)$$

yielding the scattered field $\underline{\mathbf{v}}_s(\underline{\mathbf{R}}, \omega)$ as

$$\underline{\mathbf{v}}_s(\underline{\mathbf{R}}, \omega) = \int \int_{S_c} [j\omega \underline{\mathbf{n}}_c' \cdot \underline{\underline{\mathbf{T}}}(\underline{\mathbf{R}}', \omega) \cdot \underline{\mathbf{G}}(\underline{\mathbf{R}} - \underline{\mathbf{R}}', \omega) + \underline{\mathbf{n}}_c' \underline{\mathbf{v}}(\underline{\mathbf{R}}', \omega) : \underline{\underline{\Sigma}}'(\underline{\mathbf{R}} - \underline{\mathbf{R}}', \omega)] dS'. \quad (32)$$

A concise derivation of the Huygens principle (32) can be found in Ref. [4]. Notice: The scattered field outside S_c , i.e. $\underline{\mathbf{v}}_s(\underline{\mathbf{R}}, \omega)$, adds to the incident field to yield the total field

$$\underline{\mathbf{v}}(\underline{\mathbf{R}}, \omega) = \underline{\mathbf{v}}_s(\underline{\mathbf{R}}, \omega) + \underline{\mathbf{v}}_i(\underline{\mathbf{R}}, \omega); \quad (33)$$

therefore, the field $\underline{\mathbf{v}}$ under the integral is the *total* field, and the same holds for $\underline{\underline{\mathbf{T}}}$.

Very often, the canonical scatterers in nondestructive material testing are cracks and voids in solids. Therefore, we confine ourselves to scatterers with stress-free boundaries, i.e. with the boundary condition $\underline{\mathbf{n}}_c \cdot \underline{\underline{\mathbf{T}}}(\underline{\mathbf{R}}, \omega) = \underline{\mathbf{0}}$, $\underline{\mathbf{R}} \in$

S_c ; then we obtain

$$\underline{\mathbf{v}}_s(\underline{\mathbf{R}}, \omega) = \int_{-\infty}^{\infty} \int_{-\infty}^{\infty} \int_{-\infty}^{\infty} \underline{\mathbf{n}}_c' \underline{\mathbf{v}}(\underline{\mathbf{R}}', \omega) : \underline{\underline{\Sigma}}'(\underline{\mathbf{R}} - \underline{\mathbf{R}}', \omega) d^3 \underline{\mathbf{R}}'. \quad (34)$$

Again, the surface deformation rate $\underline{\mathbf{n}}_c' \underline{\mathbf{v}}(\underline{\mathbf{R}}', \omega)$ implies the *total* field.

What are the problems with the applications of Eq. (34) to defect scattering in anisotropic materials?

1. The Green tensor $\underline{\underline{\Sigma}}'$, and because of its definition (29), the Green tensor $\underline{\underline{\mathbf{G}}}$, has to be known; we have already pointed out that this is only true for *isotropic* materials, even though some progress has been made to derive at least integral representations for Green tensors in anisotropic materials [7,10–13]. Notice: The knowledge of $\underline{\underline{\mathbf{G}}}$ is also required in the Point Source Synthesis Model (25) for $\underline{\mathbf{v}}_i$.
2. The total field $\underline{\mathbf{v}}$ has to be known on the scattering surface S_c , but $\underline{\mathbf{v}}_s$ has yet to be computed via Eq. (34); therefore, Eq. (34) serves to enforce the inherent boundary condition giving rise to integral equations for $\underline{\mathbf{v}}$ on S_c , which have then to be solved numerically (Boundary Element Method; [13,14]).

Recognizing that the Boundary Element Method requires tedious numerical calculations, one restricts to “guesses” and approximations of $\underline{\mathbf{v}}$ on S_c , in particular with the arguments of Physical Elastodynamics, which are borrowed from Kirchhoff’s Physical Optics approximation in electromagnetics (NDE applications for isotropic materials: [15–18]). If Physical Elastodynamics comes with approximations of Green’s tensors—for instance, the far-field approximation [19]—one arrives at effective computational schemes even for NDE modeling of *anisotropic* materials ([21]; strictly speaking, this is an *approximate* Point Source Synthesis Model, *not* a generalization; it might only be called a generalization regarding the previous restriction of the *approximate* Point Source synthesis Model to *isotropic* materials).

Not only that the elastodynamic Huygens principle serves as a starting point for approximate ultrasonic modeling tools, it has a tremendous potential and value to arrive at a physical intuitive understanding and explanation of elastic wave propagation in anisotropic materials. Again this physical understanding is based upon guesses of $\underline{\mathbf{v}}$ on S_c in Eq. (34)—or prescriptions of $\underline{\mathbf{f}}$ in Eq. (27)—together with a physical “realization” of the wavefronts of point sources, i.e. Green’s tensors. It turns out that these “wave surfaces” coincide with the group velocity diagrams of *plane* waves [7,8,22], thus revealing the *physics* behind these diagrams. We will compute and display, i.e. realize,

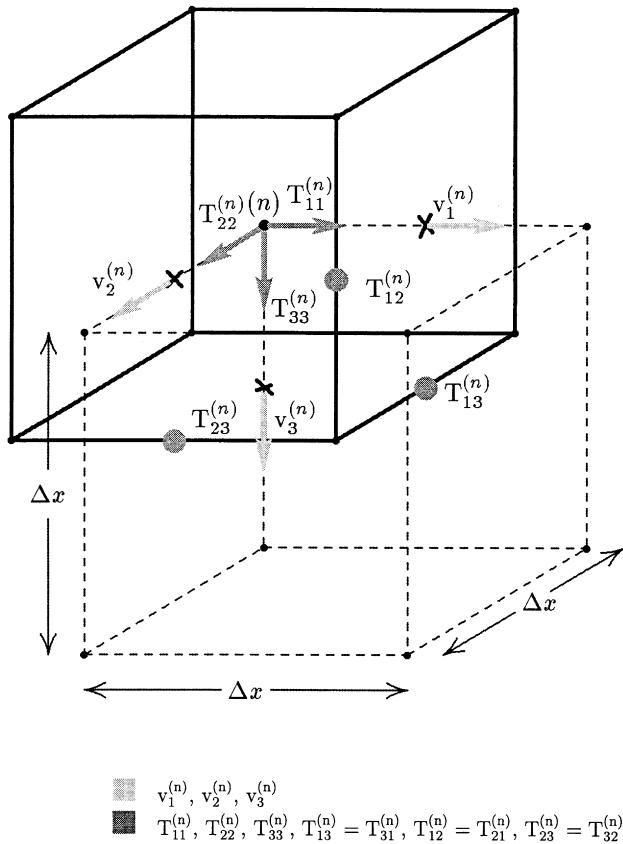


Fig. 3. The staggered grid for EFIT.

these wave surfaces with the help of a numerical method, the EFIT.

2. Elastodynamic Finite Integration Technique: EFIT

EFIT is based on an integral form of the governing equations of elastodynamics, which is obtained integrating Eqs.(1) and (2) over a volume V with closed surface S_g

and utilizing Gauss' theorem—for simplicity, sources are ignored:

$$\iint_{S_g} \underline{\mathbf{n}} \cdot \underline{\mathbf{T}}(\underline{\mathbf{R}}, t) dS = \iiint_V \frac{\partial}{\partial t} \underline{\mathbf{j}}(\underline{\mathbf{R}}, t) dV, \quad (35)$$

$$\iint_{S_g} \frac{1}{2} \{ \underline{\mathbf{n}} \underline{\mathbf{v}}(\underline{\mathbf{R}}, t) + [\underline{\mathbf{n}} \underline{\mathbf{v}}(\underline{\mathbf{R}}, t)]^{21} \} dS = \iiint_V \frac{\partial}{\partial t} \underline{\mathbf{S}}(\underline{\mathbf{R}}, t) dV. \quad (36)$$

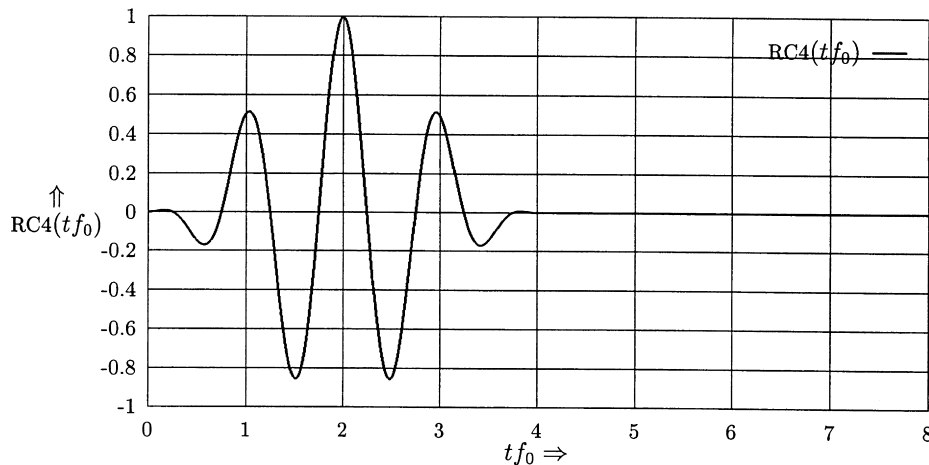
Applying the Finite Integration Technique to Eqs. (35) and (36), components of $\underline{\mathbf{T}}$ and $\underline{\mathbf{v}}$, for instance, have to be allocated as shown in Fig. 3.

Additionally, discretization of inhomogeneous materials is stringent, and that way, a consistent and convergent numerical algorithm is obtained once the stability criterion relating space and time discretization is satisfied [22]. Concerning errors, the EFIT-code is second order in space and time. Present 2D- and 3D-versions of EFIT allow for the modeling of inhomogeneous-anisotropic materials [23]. And recently, an extension to PFIT has been developed to account for coupling between electromagnetics and elastodynamics through the piezoelectric effect [23]; that way, it is principally possible to model real life piezoelectric transducers.

EFIT has been validated against a large number of analytical and experimental results [24,25].

3. EFIT and Huygens' principle: transducer radiation into anisotropic materials

As has been pointed out already, a “visualization” of the elementary elastodynamic wavelets, the wave surfaces, is required in order to apply Huygens' principle to the superposition of point sources located within a finite aperture, thus modeling a transducer. And, in fact, EFIT is *the* appropriate tool to visualize such wave surfaces [23]. According to Eq. (27), we have to choose a time function $f(t)$ for the wavelet; one of our standard impulses for such purposes, an

Fig. 4. RC4-pulse as a model for broadband transducer signals (f_0 is the center frequency).

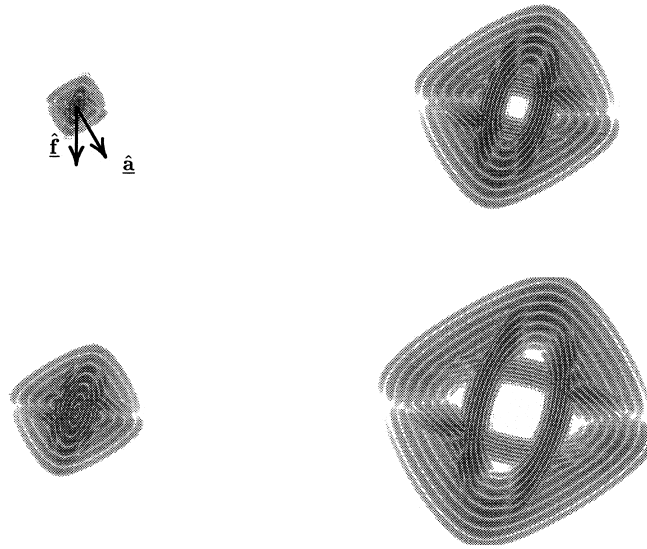


Fig. 5. 2D-EFIT-simulation of a line source in a transversely isotropic material of infinite extent (wavefronts for various fixed times).

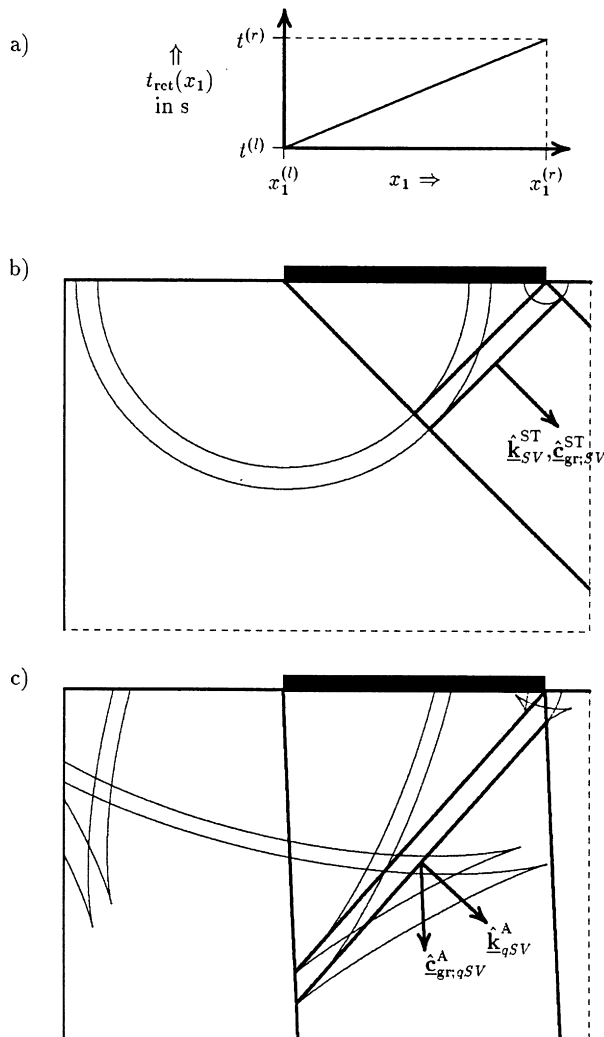


Fig. 6. Huygens-construction of a transducer beam radiating into an isotropic material and into a transversely isotropic material: (a) time retardation; (b) isotropic steel ST; (c) austenitic steel A.

RC4-pulse (raised cosine with four cycles) modeling the response of a commercial broadband piezoelectric transducer (MWB45-2) is displayed in Fig. 4. Fig. 5 exhibits wavefronts output of EFIT for an austenitic steel (modeled as transversely isotropic with given $\hat{\mathbf{a}}$ as indicated), where $\hat{\mathbf{f}}$ models a line source with $\hat{\mathbf{f}}$ as indicated; the EFIT-simulation is two-dimensional (2D) in the $\hat{\mathbf{f}}\hat{\mathbf{a}}$ -plane. It is obvious from the comparison with Fig. 2, that the wave surfaces of qP- and qSV-waves are the (energy) group velocity diagrams (notice: SH-waves are not excited for this line source excitation)! With that knowledge we can now construct a transducer beam in austenitic steel through the superposition of wave surfaces from point (line) sources within a finite aperture: Fig. 6 compares this Huygens-type construction for the 2D model of *line* sources with equal amplitudes, the aperture $x_1^{(l)} \leq x_1 \leq x_1^{(r)}$ indicated by the black bar, for *isotropic* (ferritic) steel (top) and *transversely isotropic* (austenitic) steel (bottom); through a linear time retardation $t_{\text{ret}}(x_1)$ of the line sources within the aperture, we “produce” a 45°-SV-beam in the isotropic material: The Huygens-construction implies drawing tangential lines to the spherical wavelets giving rise to an energy beam $\hat{\mathbf{c}}_{\text{gr},\text{SV}}$ which has the same direction as the normal $\hat{\mathbf{k}}_{\text{SV}}$ to the phase fronts (the tangent lines), i.e. the phase propagation direction. In opposition to that, the same Huygens-type construction based on the appropriate wave surfaces as visualized by EFIT and computed as a qSV-energy velocity diagram yields $\hat{\mathbf{c}}_{\text{gr},\text{qSV}} \neq \hat{\mathbf{k}}_{\text{qSV}}$: The 45° *phase* orientation in the beam is maintained—it is enforced by $t_{\text{ret}}(x_1)$ —but the energy, and hence, the *beam*, travels nearly orthogonal to the aperture: What was not visible for *plane* waves (Fig. 2) now becomes obvious for *beams*.

Of course, the Huygens-construction of ultrasonic beams in anisotropic materials does not account for amplitudes; it “only” serves as an intuitive way of understanding strange

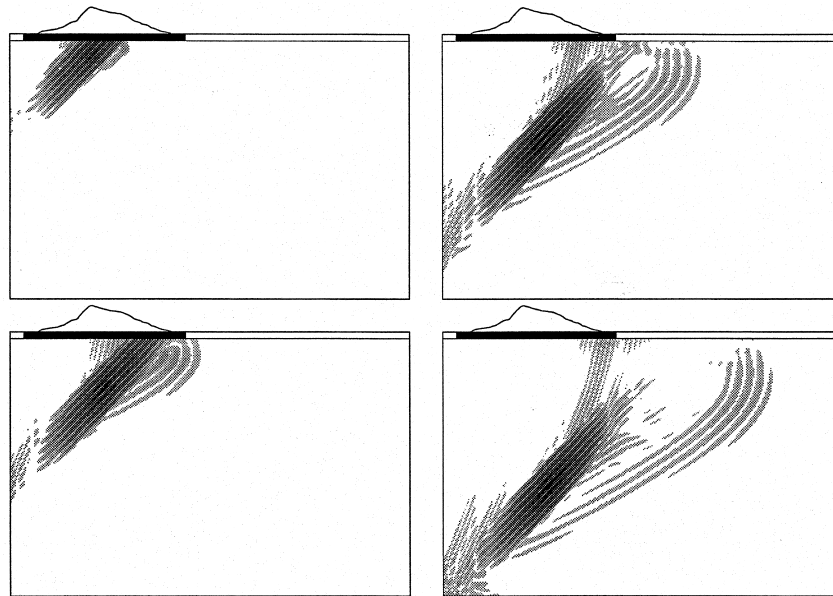


Fig. 7. 2D-EFIT impulsive transducer modeling in transversely isotropic materials.

ultrasound paths in these materials, but as such, we consider it to be of tremendous importance.

Amplitudes in the ultrasonic beam can be supplied essentially by two methods: evaluate the Point (Line) Source Synthesis integrals (25) or (32) via approximate expressions for the Green functions [20,21] (approximate analytical method) or apply EFIT to the same prescription of source distributions (“exact” numerical method).

The output of EFIT for the example of Fig. 6 is given in Figs. 7 and 8 for a MWB45-2 transducer, where we also applied a measured traction force distribution within the transducer aperture. Fig. 7 displays ultrasonic RC4-qSV-

wavefronts as snapshots, Fig. 8 shows qSV-wavefronts for a time harmonic excitation function $f(t)$ with a given switch-on time thus “reproducing” the Huygens-beam of Fig. 6.

4. Experimental validation; modeling results for various weld geometries and structures

4.1. Experimental validation

Of course, a tool such as EFIT is most powerful to model real-life ultrasonic testing situations, but, as a matter of fact,

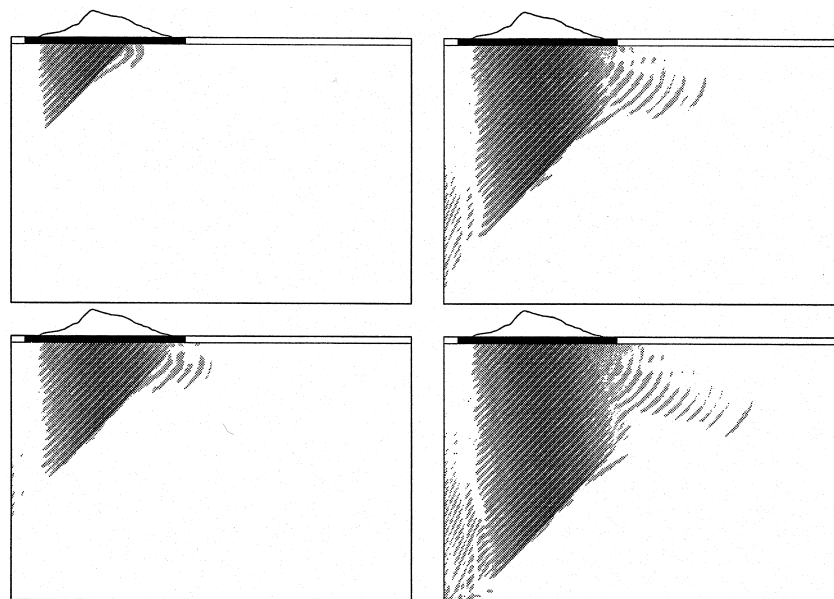


Fig. 8. 2D-EFIT monofrequent transducer modeling in transversely isotropic materials.

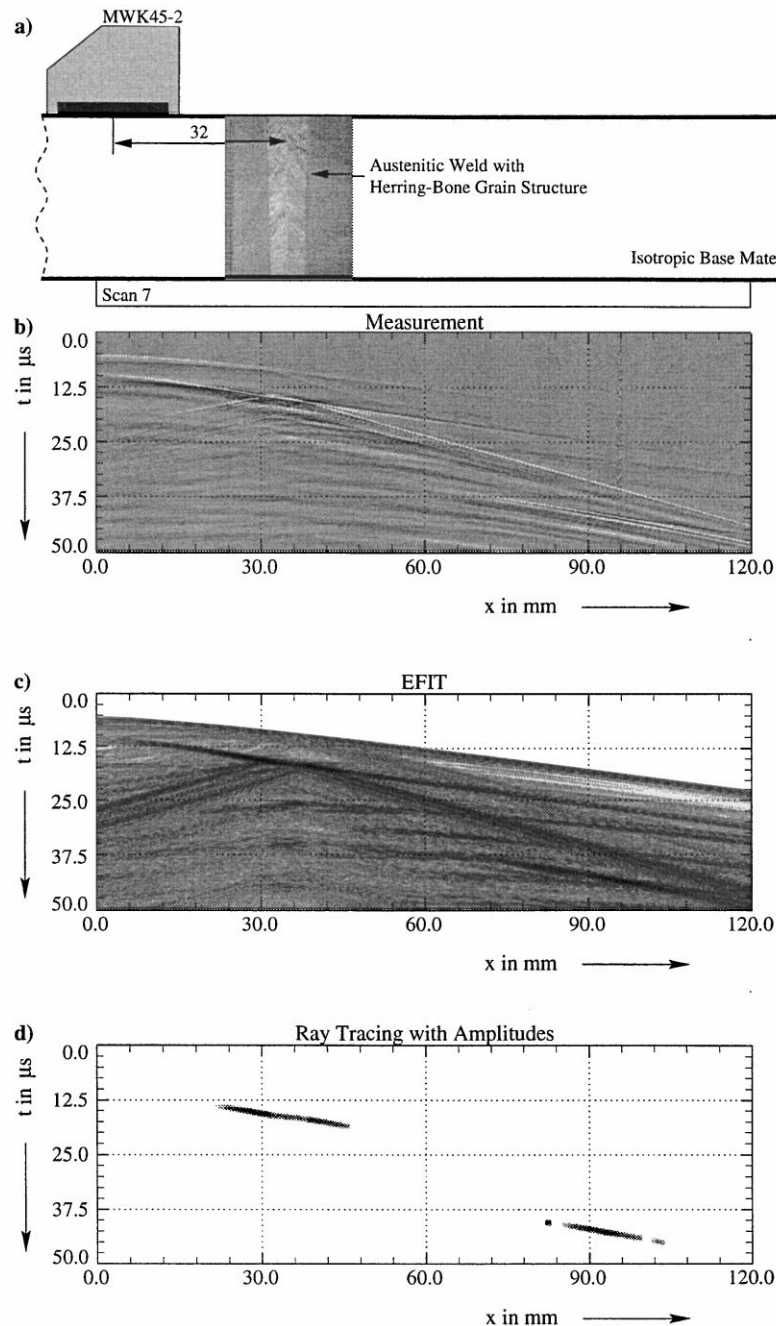


Fig. 9. Transmission through a narrow-gap weld with a herring-bone grain structure: (a) geometry and photograph of the weld; (b) experimental results; (c) EFIT modeling; (d) ray tracing modeling results.

validation is mandatory. This has two aspects: validation of the code—in particular its numerical accuracy—and validation of the physical model—for instance of the anisotropic weld structure under concern. We have checked that against a “canonical” experiment, the ultrasonic transmission through a narrow-gap weld with a herring-bone structure of the crystal grain orientation [26]. Fig. 9 exhibits the geometry under concern; a photograph of the weld structure gives rise to the particular herring-bone grain orientation in our model, which combines two transversely

isotropic materials with the previously chosen elastic constants of austenitic steel. The transducer is a commercial 45° -shear wave transducer designed for “standard” ferritic steel; in this experiment it is located at the indicated position close to the weld with some overlap (other positions are shown in Ref. [26]). The EFIT-model of the transducer is the one discussed in the previous section. Fig. 10 displays the resulting 2D-EFIT-wavefronts for the pulse-excitation given in Fig. 4; notice: There is a P-wave precursor near the specimen surface, because the 45° -SV-wave is accompanied

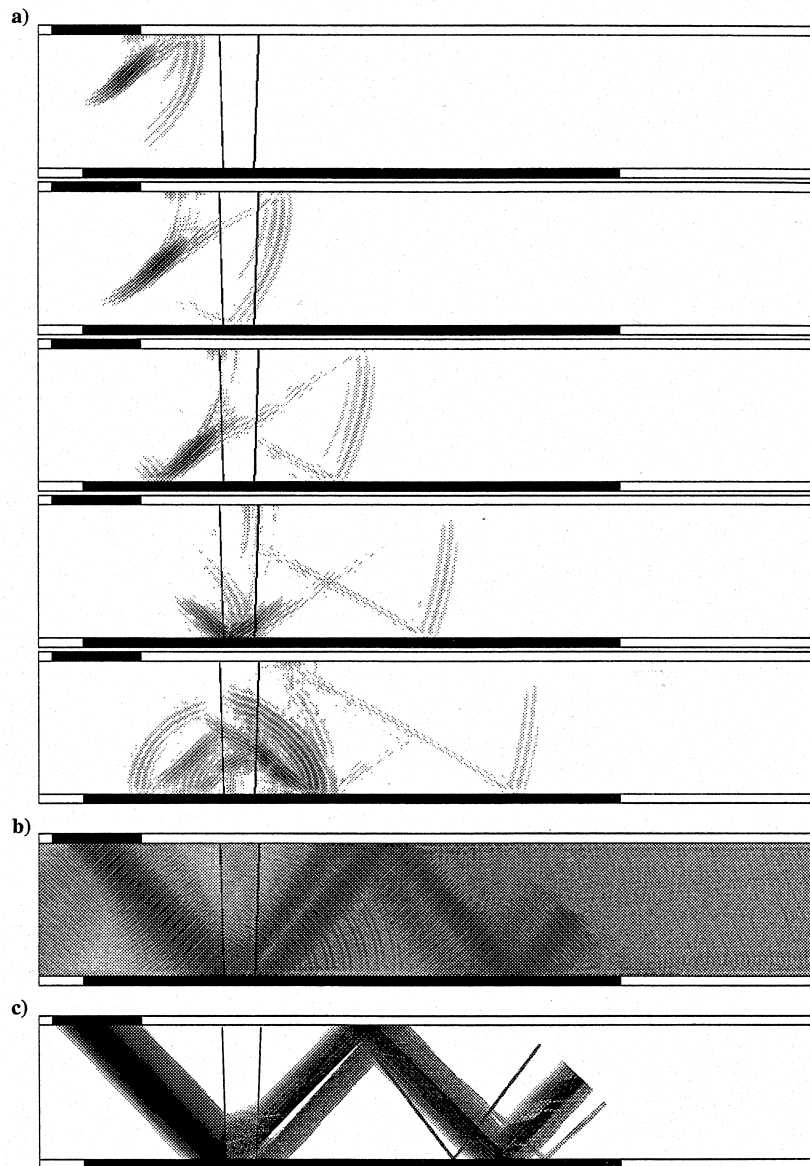


Fig. 10. 2D-EFIT-wavefronts (a) for the ultrasonic testing situations of Fig. 9, together with "EFIT-ray-tracing" (b) and "true" ray tracing (c).

by a pressure wave beyond its respective critical angle. The snapshots clearly visualize the physics of elastic wave propagation through the weld; because of the narrow weld geometry the particular effects of the anisotropic material are not really obvious in this scale, but they determine the details of the "B-scan"-like data which are displayed in Fig. 9: Ultrasonic signals recorded on the backwall of the specimen within the indicated scan aperture with a very small probe are stacked as A-scans. The topmost B-scan shows the experimental results, the one below the EFIT-modeling results, and the bottom "data" have been obtained with a ray tracing algorithm taking into account amplitudes according to plane wave theory [27], i.e. starting with a ray bundle from the transducer aperture and tracing it through boundaries with plane wave transmission coefficients disregarding reflections; Fig. 10 displays these rays

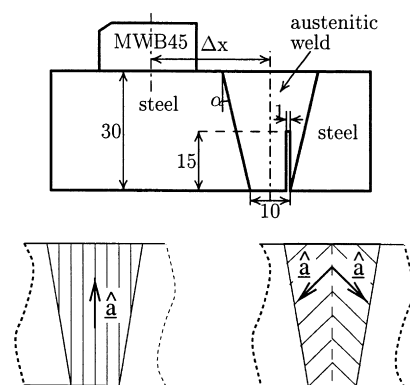


Fig. 11. Parametric weld geometry; two models for austenitic weld structure.

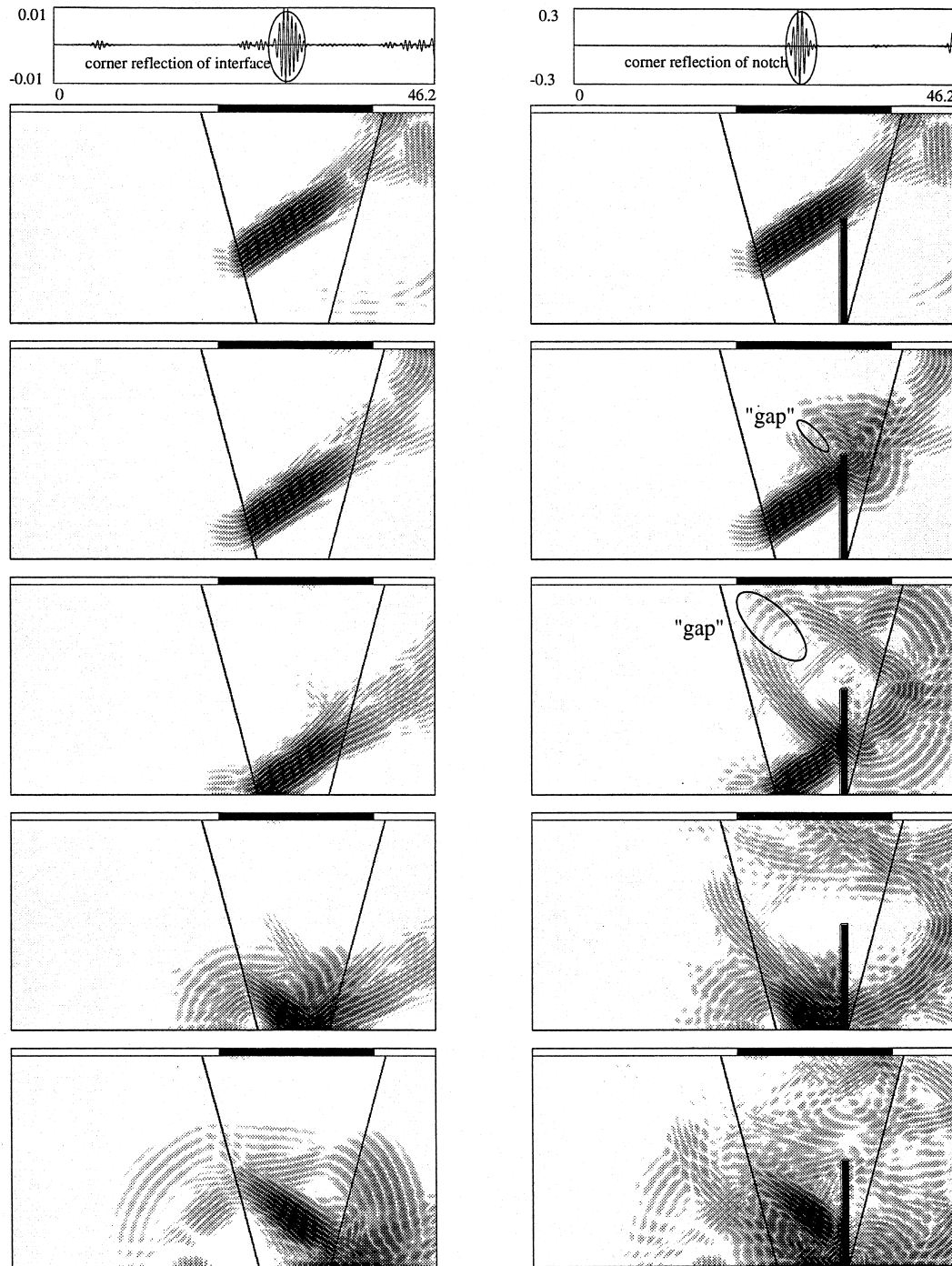


Fig. 12. 2D-EFIT-modeling results for the weld with parallel grains orthogonal to the surface ($\alpha = 15^\circ$; transducer position indicated by the bar); left: no notch, right: notch present.

in the bottom figure below the EFIT-ray-tracing through superposition of broadband wavefronts. We emphasize, that Fig. 9 clearly validates the numerical EFIT results: every single fine structure in the B-scan is present in the experiment. Of course, ray tracing, even though a powerful and fast approximate computational scheme, is only able to produce the signals from the specular reflection of the SV-wave at the backwall.

4.2. Parametric modeling study of weld geometries and structures with and without defects

Fig. 11 indicates important parameters of a weld: the angle α of the weld boundary inclination, the transducer position as counted by Δx from the middle of the weld, and two structural models, one with parallel grain orientation orthogonal to the surface, and one with the

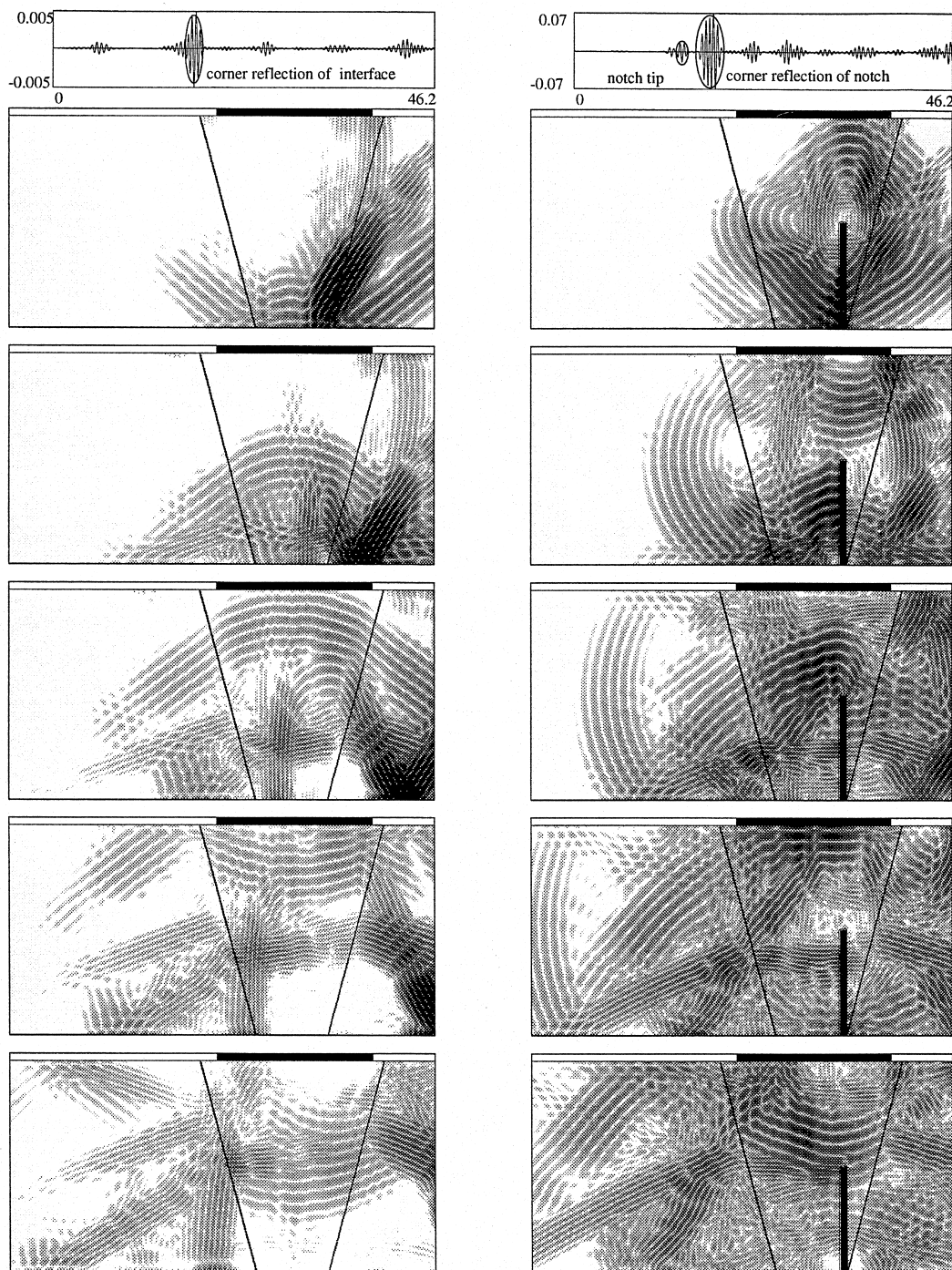
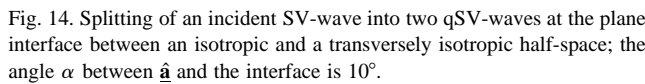


Fig. 13. 2D-EFIT-modeling results for the weld with the herring-bone structure ($\alpha = 15^\circ$; transducer position indicated by the bar); left: no notch; right: notch present.

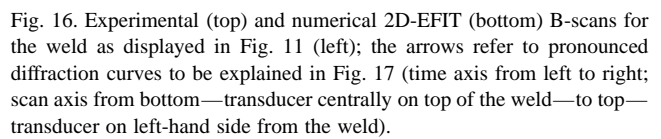
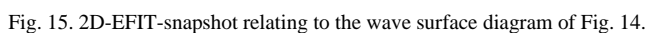
already introduced herring-bone structure. The width of the weld at the backwall and the thickness of the specimen, as well as the transducer parameters (the same as in the previous section) are kept fixed. Notice: In contrast to the previous section, the weld is *not* a narrow gap. We performed a parametric 2D-EFIT-study varying only *one* of the parameters at a time; the same parametric variation

was then repeated in the presence of a backwall breaking notch of fixed depth [28].

Figs. 12 and 13 compare the two weld structures with regard to the observability of potential notch tip echoes. In Fig. 12, the parallel grain structure is investigated, and this time, we do not only compare wavefronts nor B-scans but single A-scans in a pulse-echo measurement simulation;



During this extensive parametric study we encountered some wave phenomena which confirmed a strange prediction made by plane wave theory for the refraction of a plane SV-wave by a plane boundary between an isotropic and a transversely isotropic solid [9,27], and which, to our



Consider Fig. 14: The horizontal coordinate axis accounts for the interface between a half-space of isotropic (above the axis) and a half-space of transversely isotropic material (below the axis). The $\hat{\mathbf{a}}$ -direction is related to the interface as indicated, i.e. it refers to an ($\alpha = 10^\circ$)-inclination between the parallel grain orientation and the weld interface of Fig. 11. For the SV-wave incident from the isotropic half-space we assume a resulting 45° -orientation of the phase vector $\underline{\mathbf{k}}_{\text{qSV}}^{\text{trans}}$ of the transmitted qSV-wave with regard to the interface *in the anisotropic half-space*, where its location on the slowness surface ($\text{qSV}^{\text{aust.}}$: dotted curve) is determined by the phase-matching condition in the interface, relating the projection of $\underline{\mathbf{k}}_{\text{qSV}}^{\text{trans}}$ (dotted line orthogonal to the interface) to the pertinent projection of the phase vector $\underline{\mathbf{k}}_{\text{SV}}^{\text{refl}}$ of the SV-wave reflected back into the isotropic half-space and being located on a *spherical* slowness surface ($\text{SV}^{\text{steel.}}$: dashed curve). The direction of the energy velocity of the transmitted qSV-wave is found as the vector $\hat{\mathbf{c}}_{\text{gr,qSV}}^{\text{trans}}$, which is orthogonal to the slowness surface at the point $\underline{\mathbf{k}}_{\text{qSV}}^{\text{trans}}$. This is the first—conventional, regular, ordinary?—qSV-wave.

In addition to the slowness surface of the qSV-wave in the anisotropic half-space we have plotted the qP-slowness surface (encircled 1), which, with increasing angle of incidence of the SV-wave beyond the critical angle of the qP-wave, exhibits, besides a real part (encircled 2), an imaginary part (encircled 3), thus defining an evanescent wave. In contrast to “ordinary” evanescent waves, the real part of the phase vector, as a solution of the pertinent eigenvalue problem, points into the upper half-space (and not along

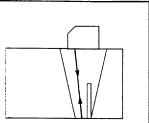
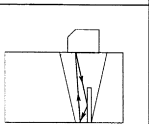
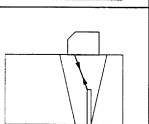
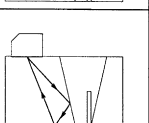
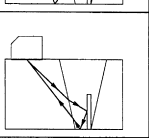
1	backwall echo of shear wave	
2	second corner reflection (of shear wave)	
3	notch tip	
4	corner reflection at front V-butt weld flank	
5	corner reflection	

Fig. 17. Icons to explain the physical origin of the diffraction curves of Fig. 16 marked by the arrows.

the interface); with further increasing angle of incidence, this real part continues its path as a *real* (vanishing imaginary part) solution on the slowness surface of the qSV-wave as if the latter would exist in the upper half-space (encircled 4), and when it reaches the “phase-matching-line”, it defines a phase vector of a second qSV-wave $\mathbf{k}_{\text{qSV}(2)}^{\text{trans}}$, whose pertinent energy velocity vector $\hat{\mathbf{c}}_{\text{gr;qSV}(2)}^{\text{trans}}$, being orthogonal to

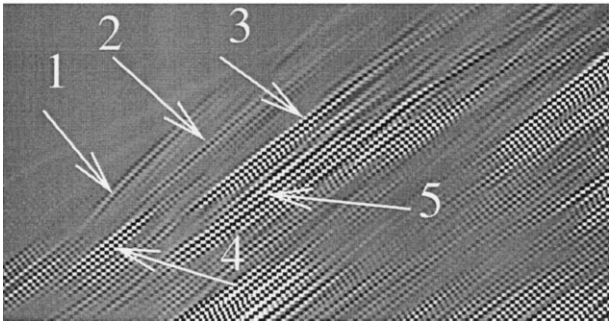
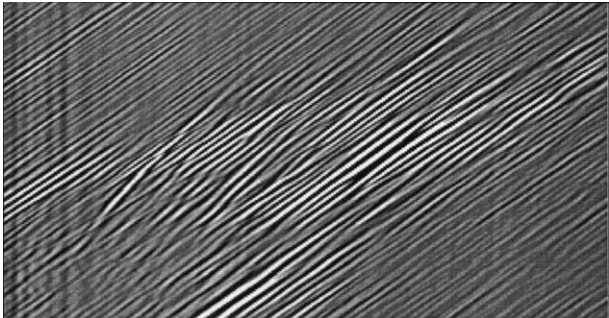
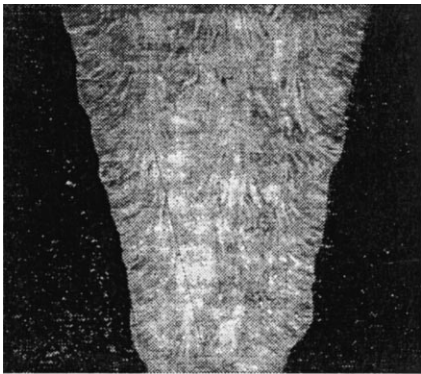


Fig. 19. Experimental (top) and numerical 2D-EFIT (bottom) B-scans for the weld as displayed in Fig. 18; the arrows refer to pronounced diffraction curves to be explained in Fig. 20 (time axis from left to right; scan axis from bottom—transducer centrally on top of the weld—to top—transducer on left-hand side from the weld).

the slowness surface, points downward to the interface, thus physically *realizing* that wave as a propagating transmitted wave. Consequently, the computed EFIT-snapshot of Fig. 15 should not come as a surprise: EFIT visualizes the

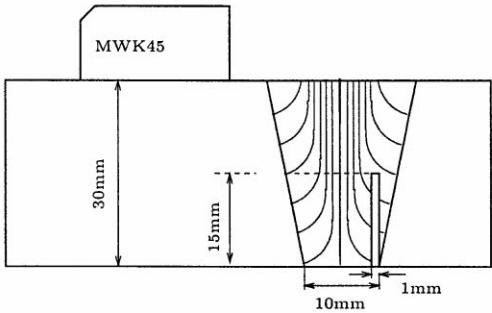
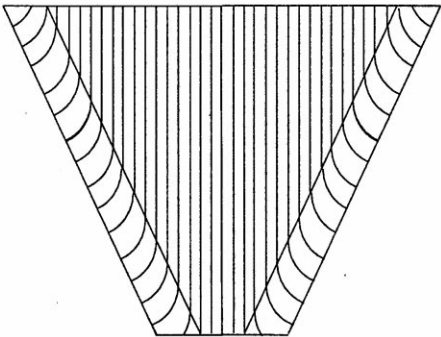


Fig. 18. Geometry and grain structure of a real-life weld.

1	modeconverted corner reflection at front V-butt weld flank	
2	modeconverted corner reflection	
3	corner reflection at front V-butt weld flank	
4	notch tip	
5	corner reflection	

Fig. 20. Icons to explain the physical origin of the diffraction curves of Fig. 19 marked by the arrows.

physics of elastic wave propagation, and, obviously, *both* transmitted qSV-waves appear at the weld interface.

4.3. Towards modeling of real-life anisotropic welds

In this section we want to confirm that a certain model

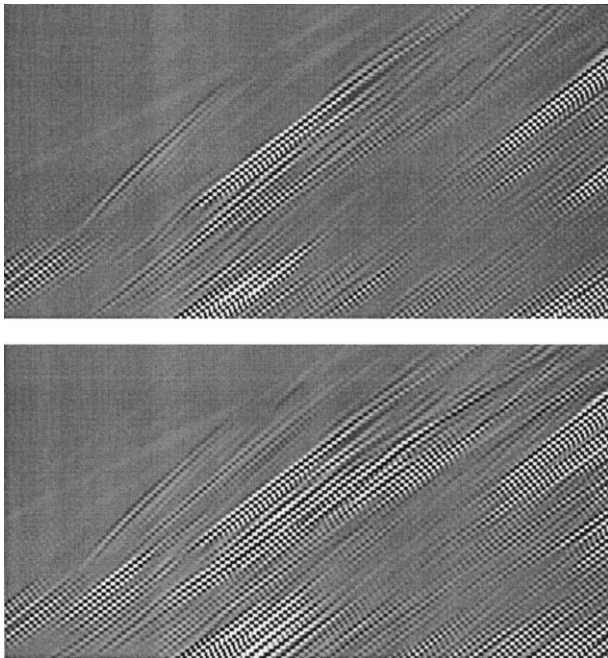


Fig. 21. 2D-EFIT-simulations of the real-life weld with (bottom) and without (top) notch (time axis from left to right; scan axis from bottom—transducer centrally on top of the weld—to top—transducer on left-hand side from the weld).

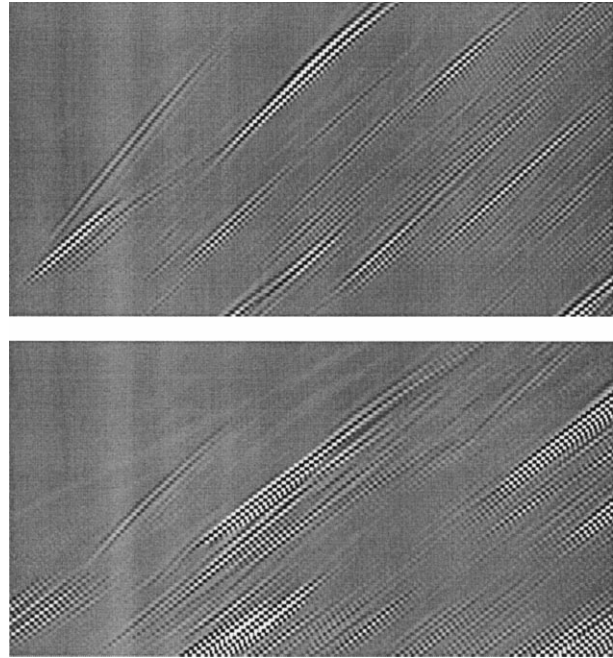


Fig. 22. Comparison of 2D-EFIT-modeled B-scans for the weld with parallel grain orientation (top) and the weld with curved grains (bottom) (time axis from left to right; scan axis from bottom—transducer centrally on top of the weld—to top—transducer on left-hand side from the weld).

deduced from a real-life weld (Fig. 18) *must* be modeled as such, it cannot be replaced by a simpler model (Fig. 11) for quantitative prediction of ultrasonic signals. We will do this in terms of numerical and experimental pulse echo B-scan results [28,29]. So, let us go back to Fig. 11, in particular to the weld structured as parallel grains orthogonal to the surface, to compute and measure B-scans in a pulse echo mode; Fig. 16 compares the results, and a very good coincidence of the main features is immediately recognized. Fig. 17 displays various icons, which explain the physical origin of the most prominent diffraction curves in Fig. 16; of course, in order to find the diffraction curve of a particular ultrasonic “ray”, it is very helpful to watch to animated wave propagation, which is the primary output of EFIT. A careful investigation of these animations revealed physical evidence of the second qSV-wave as discussed in the previous section (arrows 6 and 7 in Fig. 16).

Fig. 18 shows the geometry and grain structure of a real-life weld together with the model we adjust to it; notice: we account for a continuous curvature of the grains, i.e. characterizing an *inhomogeneous* transversely isotropic material. The B-scan results of the experiment and the 2D-EFIT-simulation are given in Fig. 19, and Fig. 20 presents the pertinent icons.

It is astonishing how well the numerical simulations reproduce the experiment; this gives confidence that modeling tools such as EFIT are not restricted to canonical testing situations with no practical relevance; in contrast to that, they prove to be a thorough means to interpret, analyze,

plan and optimize ultrasonic testing of real-life austenitic welds.

Therefore, Fig. 21 *confirms* via simulations that a notch corner as well as its tip is clearly visible in the B-scan of the real-life weld.

Fig. 22 presents *the* crucial result: It compares the modeled B-scans for the weld with purely parallel grain orientation with the one for the weld with curved grain orientation, and, obviously, it is a *must* to model the real-life weld as it is, and not in a downgraded approximation.

References

- [1] Achenbach JD. Wave propagation in elastic solids. Amsterdam: North-Holland, 1973.
- [2] Auld BA. Acoustic fields and waves in solids, vols. I and II. New York: Krieger, 1990.
- [3] de Hoop AT. Handbook of radiation and scattering of waves. London: Academic Press, 1995.
- [4] Langenberg KJ, Fellinger P, Marklein R, Zanger P, Mayer K, Kreutter T. Inverse methods and imaging. In: Achenbach JD, editor. Evaluation of materials and structures by quantitative ultrasonics, Vienna: Springer, 1993.
- [5] Langenberg KJ, Brandfass M, Hannemann R, Hofmann C, Kaczorowski T, Kostka J, Marklein R, Mayer K, Pitsch A. Inverse scattering with acoustic, electromagnetic, and elastic waves as applied in nondestructive evaluation. In: Wirgin A, editor. Scalar and vector wavefield inverse problems, Vienna: Springer, 1999.
- [6] Spies M. Elastic waves in homogeneous and layered transversely isotropic media: plane waves and Gaussian wave packets. J. Acoust. Soc. Am. 1994;95:1748–60.
- [7] Nayfeh AH. Wave propagation in layered anisotropic media. Amsterdam: North-Holland, 1995.
- [8] Helbig K. Foundations of anisotropy for exploration seismics. New York: Pergamon Press, 1994.
- [9] Neumann E. Ultraschallprüfung von austenitischen Plattierungen, Mischnähten und austenitischen Schweißnähten. Renningen-Malmsheim: Expert Verlag, 1995.
- [10] Spies M. Elastic wave propagation in general transversely isotropic media: Green's functions and elastodynamic holography. J Acoust Soc Am 1994;96:1144–57.
- [11] Wang CY, Achenbach JD. Three-dimensional time-harmonic elastodynamic Green's function for anisotropic solids. Proc R Soc London, A 1995;449:441–58.
- [12] van der Hijden JHMT. Propagation of transient elastic waves in stratified anisotropic media. Amsterdam: North-Holland, 1987.
- [13] Mattson J, Niklasson AJ, Eriksson A. Three-dimensional ultrasonic crack detection in anisotropic materials. Res Nondestr Eval 1997;9:59–79.
- [14] Wang CY, Achenbach JD, Hirose S. Two-dimensional time domain BEM for scattering of elastic waves in solids of general anisotropy. Int J Solids Struct 1996;33:3843–64.
- [15] Schmerr Jr. LW. Fundamentals of ultrasonic nondestructive evaluation. New York: Plenum Press, 1998.
- [16] Harker AH. Elastic waves in solids, British gas. Bristol: Adam Hilger, 1988.
- [17] Boehm R, Erhard A, Wüstenberg H. Darstellung des Entwicklungsstandes des schnellen halbanalytischen Modells (FSAM) für die Ultraschallprüfung anhand von Beispielen. Berichtsband zur Jahrestagung der Deutschen Gesellschaft für Zerstörungsfreie Prüfung, Celle 1999;317–26.
- [18] Paradis L, Talvard M, Rizo P, Pascal G, Bayon G, Benoist P. CEA program for multiple-technique nondestructive testing: the CIVA system. In: Thompson DO, Chimenti DE, editors. Review of progress of QNDE, vol. 17. New York: Plenum Press, 1998.
- [19] Buchwald VT. Elastic waves in anisotropic media. Proc R Soc London, A 1959;253:563–80.
- [20] Spies M. Transducer-modeling in general transversely isotropic media via point-source-synthesis. Theory J Nondestr Eval 1994;13:85–99.
- [21] Spies M, Walte F. Application-directed modeling of radiation and propagation of elastic waves in anisotropic media: GPSS and OPoSSM. In: Thompson DO, Chimenti DE, editors. Review of progress in QNDE, vol. 14. New York: Plenum Press, 1995.
- [22] Fellinger P, Marklein R, Langenberg KJ, Klaholz S. Numerical modeling of elastic wave propagation and scattering with EFIT-Elastodynamic Finite Integration Technique. Wave Motion 1995;21:47.
- [23] Marklein R. Numerische Verfahren zur Modellierung von akustischen, elektromagnetischen, elastischen und piezoelektrischen Wellen-ausbreitungsproblemen im Zeitbereich basierend auf der Finiten Integrationstechnik. Aachen: Shaker Verlag, 1997.
- [24] Marklein R, Langenberg KJ, Klaholz S, Kostka J. Ultrasonic modeling of real-life NDT situations: applications and further developments. In: Thompson DO, Chimenti DE, editors. Review of progress of quantitative NDE, vol. 15. New York: Plenum Press, 1996. p. 57.
- [25] Walte F, Schurig C, Spies M, Langenberg KJ, Klaholz S. Experimental evaluation of ultrasonic simulation techniques in anisotropic material. In: Thompson DO, Chimenti DE, editors. Review of progress of quantitative NDE, vol. 16. New York: Plenum Press, 1997. p. 1899.
- [26] Marklein R, Kaczorowski T, Hannemann R, Langenberg KJ. Modellierung der Ultraschallausbreitung in austenitischen Schweißverbindungen—Strahlenverfolgung (ray tracing) gegenüber EFIT. Berichtsband 63.2 zur Jahrestagung der Deutschen Gesellschaft für Zerstörungsfreie Prüfung, Bamberg, 1998.
- [27] Rokhlin SI, Bolland TK, Adler L. Reflection and refraction of elastic waves on a plane interface between two generally anisotropic media. J Acoust Soc Am 1986;79(14):906–18.
- [28] Hannemann R, Marklein R, Langenberg KJ. Numerical modeling of elastic wave propagation in inhomogeneous anisotropic media. Proceedings of the Seventh European Conference on Nondestructive Testing, Copenhagen, 1998.
- [29] Hannemann R, Marklein R, Kaczorowski T, Langenberg KJ, Schurig C, Köhler B, Walte F. Ultraschall-Impulsechopprüfung austenitischer schweißnähte: Vergleich von Simulation und Messung. Berichtsband zur Jahrestagung der Deutschen Gesellschaft für Zerstörungsfreie Prüfung, Celle 1999;327–35.